Orthorhombic-to-tetragonal transition of SrRuO3 layers in Pr0.7Ca0.3MnO3/SrRuO3 superlattices

M Ziese, I Vrejoiu, E Pippel, A Hähnel, E Nikulina, D Hesse

Orthorhombic-to-tetragonal transition of $SrRuO_3$ layers in $Pr_{0.7}Ca_{0.3}MnO_3/SrRuO_3$ superlattices

M Ziese[a], I Vrejoiu[b], E Pippel[b], A. Hähnel[b], E Nikulina[b,c] and D Hesse[b]

[a] Division of Superconductivity and Magnetism, Faculty of Physics and Geosciences, University of Leipzig, 04103 Leipzig, Germany

[b] Max Planck Institute of Microstructure Physics, 06120 Halle, Germany

[c] Present address: CIC nanoGUNE Consolider, Tolosa Hiribidea 76, 20018 Donostia-San Sebastián, Spain

E-mail: ziese@physik.uni-leipzig.de

E-mail: vrejoiu@mpi-halle.mpg.de

Abstract. High-quality $Pr_{0.7}Ca_{0.3}MnO_3/SrRuO_3$ superlattices with ultrathin layers were fabricated by pulsed laser deposition on $SrTiO_3$ substrates. The superlattices were studied by atomically resolved scanning transmission electron microscopy, high-resolution transmission electron microscopy, resistivity and magnetoresistance measurements. The superlattices grew coherently without growth defects. Viewed along the growth direction, $SrRuO_3$ and $Pr_{0.7}Ca_{0.3}MnO_3$ layers were terminated by RuO_2 and MnO_2, respectively, which imposes a unique structure to their interfaces. Superlattices with a constant thickness of the $SrRuO_3$ layers, but varying thickness of the $Pr_{0.7}Ca_{0.3}MnO_3$ layers showed a change of crystalline symmetry of the $SrRuO_3$ layers. At a low $Pr_{0.7}Ca_{0.3}MnO_3$ layer thickness of 1.5 nm transmission electron microscopy proved the $SrRuO_3$ layers to be orthorhombic, whereas these were non-orthorhombic for a $Pr_{0.7}Ca_{0.3}MnO_3$ layer thickness of 4.0 nm. Angular magnetoresistance measurements showed orthorhombic (with small monoclinic distortion) symmetry in the first case and tetragonal symmetry of the $SrRuO_3$ layers in the second case. Mechanisms driving this orthorhombic to tetragonal transition are briefly discussed.

Submitted to: *JPD*

PACS numbers: 75.70.Cn, 75.47.-m, 75.47.Lx, 75.30.Gw, 68.37.-d

1. Introduction

Heterostructures and superlattices (SLs) of oxide perovskites open an exciting field of research, since it is possible by present epitaxy techniques to grow samples with clearly defined interfaces allowing for the realization of new functionalities. Some examples are the two-dimensional electron gas at the $SrTiO_3$-$LaAlO_3$ interface [1], electron tunnelling in multiferroic systems [2], growth of extrinsic multiferroic superlattices [3], as well as the observation of a giant interlayer exchange coupling in $La_{0.7}Sr_{0.3}MnO_3/SrRuO_3$ superlattices [4, 5]. The latter exchange coupling leads to positive exchange bias [6, 7, 8] and is mediated by the direct Mn-O-Ru-bond [4, 9]. The exchange bias is very large, since the individual layer thickness in the SLs is very small. In general, in systems with strong correlations between the electronic, magnetic and structural degrees of freedom one would expect to find new phenomena in the limit of ultrathin layers, i.e. in restricted geometries.

In this paper, another type of perovskite superlattice is studied, consisting out of ultrathin $Pr_{0.7}Ca_{0.3}MnO_3$ (PCMO) and $SrRuO_3$ (SRO) layers. Bulk SRO is an itinerant ferromagnet with orthorhombic crystal structure (space group Pbnm, lattice parameters $a = 0.55670$ nm, $b = 0.55304$ nm, $c = 0.78446$ nm) and a Curie temperature of about 160 K [10, 11]. Bulk PCMO has orthorhombic symmetry (Pbnm, $a = 0.5426$ nm, $b = 0.5478$ nm, $c = 0.7679$ nm); it has a complex magnetic behavior and phase diagram, and for 30% Ca doping several transitions occur upon cooling, with an insulating canted ferromagnetic or antiferromagnetic state below $\simeq 110$ K [12, 13]. The aim of this work is to investigate the crystalline symmetry of the individual layers. This is a formidable task, since the layer thickness is below 5 nm and since the orthorhombic distortions from the pseudocubic cell are at maximum 0.3% for SRO and 0.6% for PCMO. This task was tackled by high-resolution transmission electron microscopy as well as angular-dependent magnetoresistance (MR) measurements. Since PCMO is insulating, the MR measurements only probe the SRO layers. We have shown before that the crystalline symmetry of orthorhombic SRO single layers could be accurately studied by angular MR measurements, revealing a monoclinic distortion of the *a*- and *b*-axes [14] that was also observed in high-resolution X-ray diffractometry [15].

2. Experimental

PCMO/SRO SLs were fabricated by pulsed-laser deposition at a temperature of 650°C and in an oxygen partial pressure of 0.14 mbar. Vicinal $SrTiO_3$ (100) single crystal substrates with a low miscut angle of about 0.1 degree were used for the growth, after being etched in buffered HF and annealed at 1000°C for 2 hours in air. This treatment assured substrate surfaces with atomically flat terraces of a width between 100 and 500 nm separated by unit-cell high steps. The SLs consisted of fifteen PCMO/SRO bilayers with various layer thicknesses, see Table 1.

High-angle annular dark-field scanning transmission electron microscopy (HAADF-

Table 1. Samples studied in this work. For all samples the Curie temperature of the SRO layers was $T_C = 143$ K and the Néel temperature of the PCMO layers was $T_N = 110$ K.

Sample	$[PCMO / SRO]_{15}$	
SL1	[1.5 nm / 4.4 nm]	[4 u.c. / 10-11 u.c.]
SL2	[3.0 nm / 4.0 nm]	[8 u.c. / 9-10 u.c.]
SL3	[3.8 nm / 4.0 nm]	[10 u.c. / 10 u.c.]

STEM), electron energy loss spectroscopy (EELS) and energy dispersive X-ray (EDX) mappings were done in a TITAN 80-300 FEI microscope (300 keV energy of the primary electrons) with a spherical aberration corrected ($c_s = 0$) probe forming system. For the related Scherzer conditions [16] used, i.e. a focus of $\Delta = c_s = 0$ nm, image aberrations were minimum and all atomic columns were clearly resolved in the HAADF-STEM mode. High-resolution transmission electron microscopy (HRTEM) investigations were performed in a Jeol 4010 (400 keV energy of the primary electrons), and Fourier-filter-related image processing was performed by help of the Digital Micrograph program package (Gatan Inc.). For magnetoresistance measurements the SLs were mounted on a rotatable stage with an angular resolution better than 0.01 degree and an angle slackness after reversal of $0.1-0.2$ degree. The measurements were performed in a He-flow cryostat equipped with an 8 T superconducting solenoid.

3. Structural properties

3.1. Interfacial structure

Figure 1 shows HAADF-STEM micrographs of the three PCMO/SRO SLs, with respective layers thicknesses of 1.5 nm/4.4 nm (SL1, Fig. 1(a)), 3.0 nm/4.0 nm (SL2, Fig. 1(b)) and 3.8 nm/4.0 nm (DL3, Fig. 1(c)). The layers were grown entirely epitaxially, with coherent interfaces between the PCMO and SRO layers. No misfit dislocations were found along the interfaces. Closer inspection of the HAADF-STEM micrographs revealed an asymmetry of the interfaces: in the growth direction, the PCMO layers terminated most probably with MnO_2 planes, and the SRO layers terminated most likely with RuO_2 planes, resulting in different interface contrasts, see Fig. 2.

3.2. Crystal symmetry of the $SrRuO_3$ layers

Fast Fourier transforms (FFTs) of HRTEM and STEM micrographs showed orthorhombic reflections indicating that either PCMO or SRO, or both, had orthorhombic structure in the SLs. Bulk PCMO and SRO have orthorhombic structures at room temperature, however, for epitaxial films, especially coherent and ultrathin

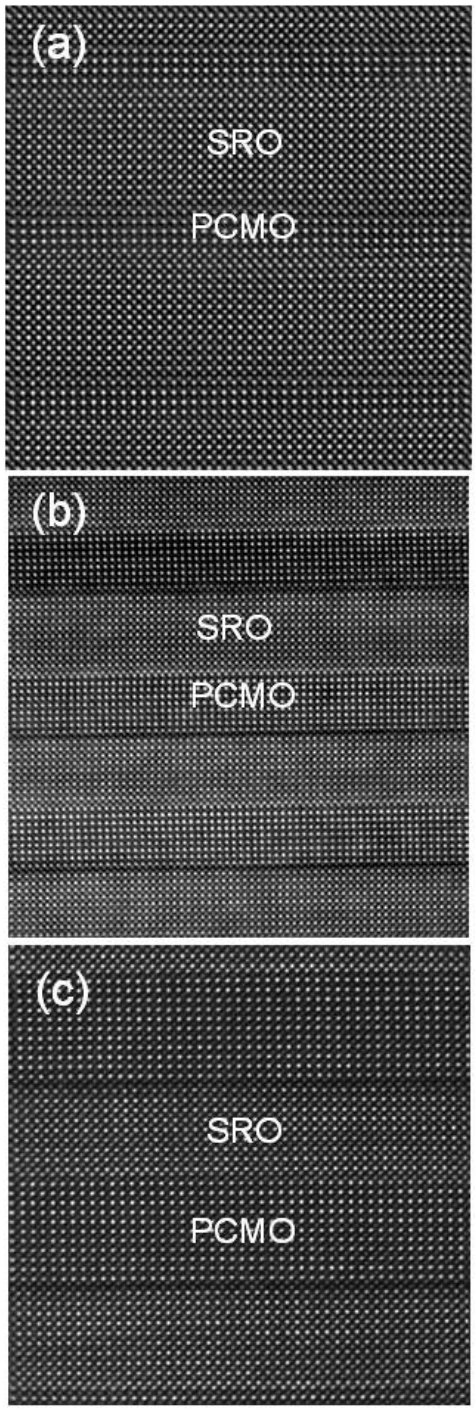

Figure 1. HAADF-STEM images of samples (a) SL1 (1.5 nm/4.4 nm), (b) SL2 (3.0 nm/4.0 nm) and (c) SL3 (3.8 nm/4.0 nm).

ones grown on dissimilar substrates, distortions from the orthorhombic bulk structure and formation of particular configurations of crystallographic domains are expected to occur [15, 17]. For example, epitaxial SRO films on $DyScO_3(110)$ were proven to have tetragonal structure [18].

Dark-field reconstructed images in the light of certain reflections, obtained from

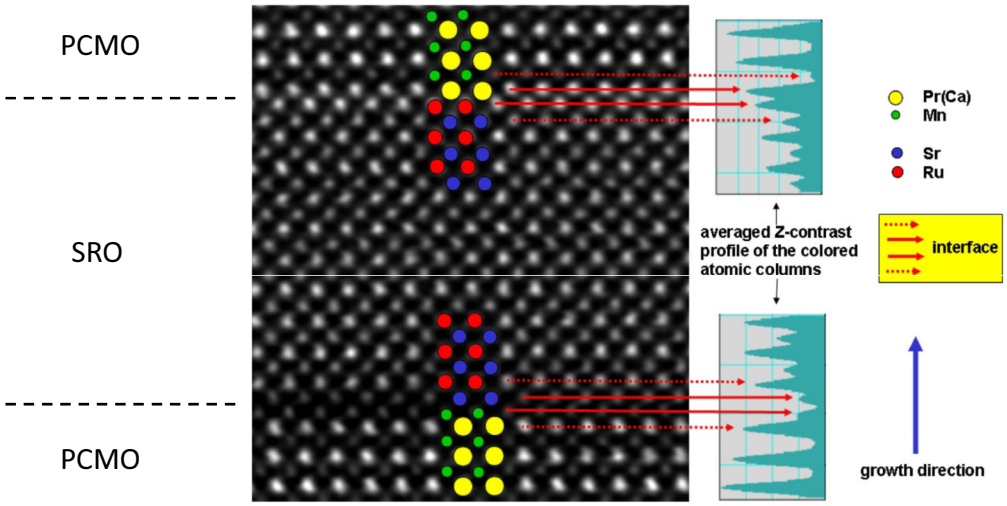

Figure 2. Z-STEM image of sample SL3 showing the interfacial structure. The intensity scans shown to the right of the image allow for a unique determination of the cation species due to the monotonic dependence of intensity on atomic number.

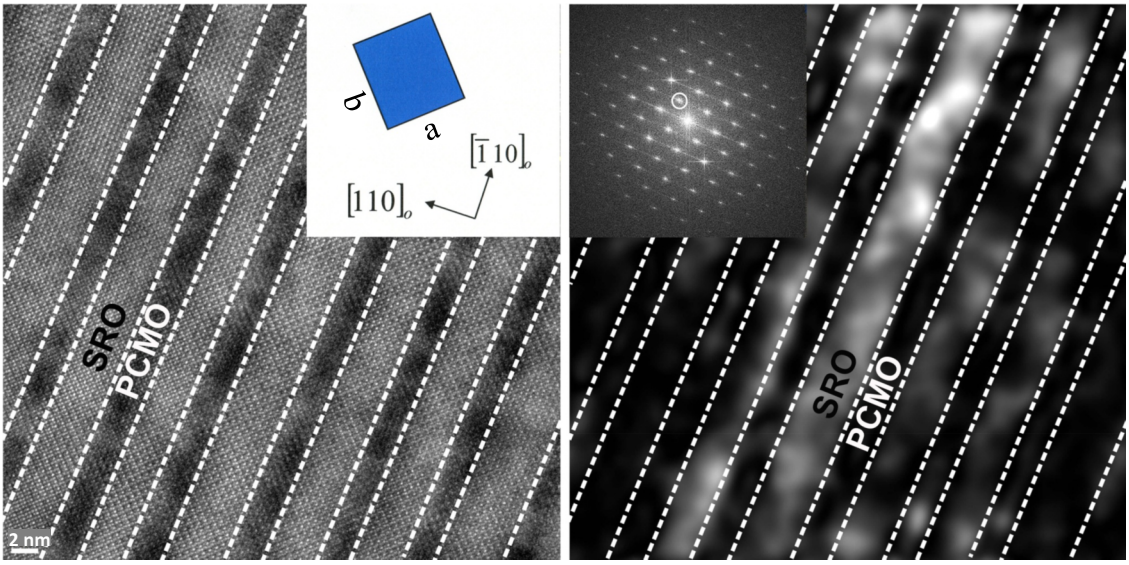

Figure 3. Sample SL1. Cross-sectional HRTEM image (left), fast-Fourier spectrum (right inset), reconstructed dark-field image in the light of the $(010)_o$ reflection (right) and scheme of the oriented projection of the orthorhombic SRO unit cell with in-plane c-axis along the viewing direction (left inset). Mind the scale bar (2 nm) in the bottom left corner.

cross-sectional HRTEM images of samples SL1 and SL3, revealed a characteristic difference between these samples: whereas the SRO layers of sample SL1 were clearly orthorhombic, with the long orthorhombic axis lying in the plane of the layers, the SRO layers in sample SL3 were either not orthorhombic or contain only very few orthorhombic domains.

HRTEM images were taken from cross sections of samples SL1 and SL3. FFTs

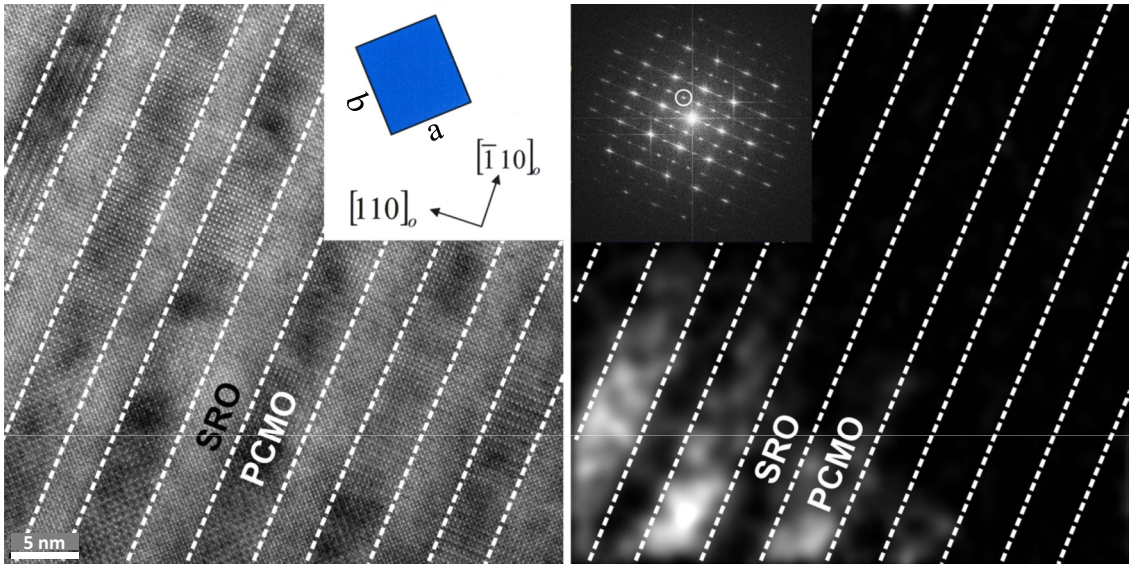

Figure 4. Sample SL3. Same as Fig. 3. Mind the scale bar (5 nm) in the bottom left corner.

and reconstructed dark-field images in the light of certain reflections were prepared. Note again that in the following the long orthorhombic axis of the SRO unit cell is defined as the *c*-axis. In particular, the following reflections were used to characterize the superlattices with respect to the presence of an orthorhombic phase in the SRO layers:

(i) the orthorhombic $(010)_o$ reflections corresponding to those parts of both SRO and PCMO lattices in which the orthorhombic *c*-axis was potentially in-plane (i.e. in the plane of the layers) along the viewing direction (Figs. 3 and 4, see insets);

(ii) the orthorhombic $(001)_o$ reflections corresponding to those parts of both SRO and PCMO lattices in which the orthorhombic *c*-axis was potentially in-plane but perpendicular to the viewing direction (Fig. 5, see inset), and

(iii) the orthorhombic $(001)_o$ reflections corresponding to those parts of both SRO and PCMO lattices in which the orthorhombic *c*-axis was potentially out-of-plane (perpendicular to the plane of the layers and perpendicular to the viewing direction) (Fig. 6, see inset).

A distinction between orthorhombic and tetragonal phases is possible for the dynamically appearing $(100)_o$, $(010)_o$ and $(001)_o$ reflections which are present in the orthorhombic phase, but absent in the tetragonal phase.

For sample SL1, in the reconstructed dark-field image of Fig. 3 (right) in the light of the $(010)_o$ reflection, the SRO layers are mostly imaged with high intensity (i.e. bright). This means that in sample SL1, the SRO layers are clearly orthorhombic, with the *c*-axis in the plane of the layers. Opposite to this, for sample SL3, in the corresponding reconstructed dark-field image of Fig. 4 (right) in the light of the $(010)_o$ reflection, the SRO layers are all imaged with very low intensity (i.e. dark). Since this could also

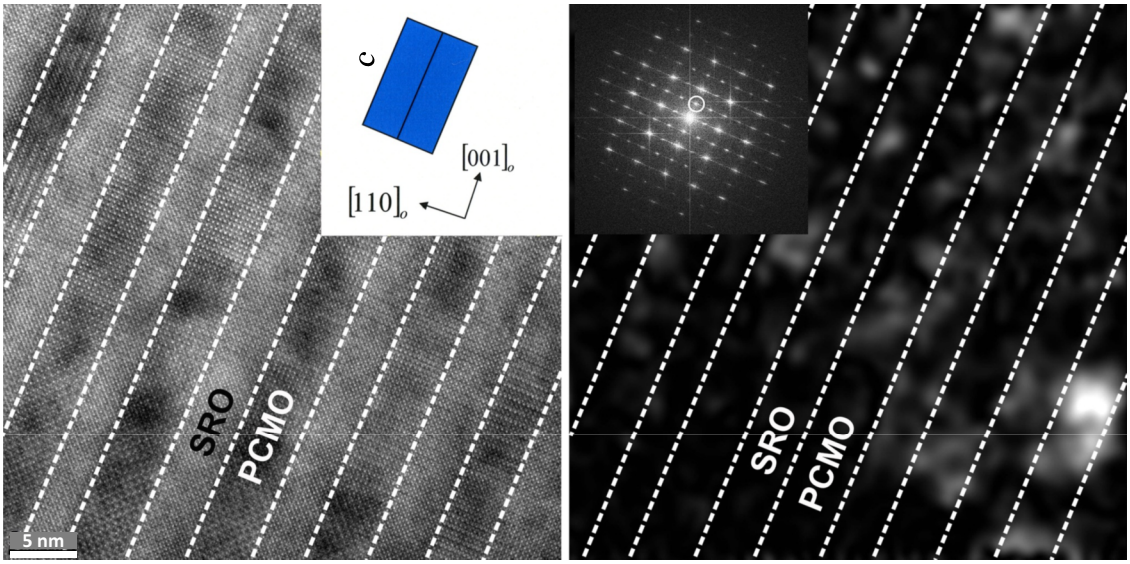

Figure 5. Sample SL3. Same as Fig. 4, but with reconstruction in the light of the $(001)_o$ reflection. *The in-plane orthorhombic c-axis is perpendicular to the viewing direction.* Mind the scale bar (5 nm) in the bottom left corner.

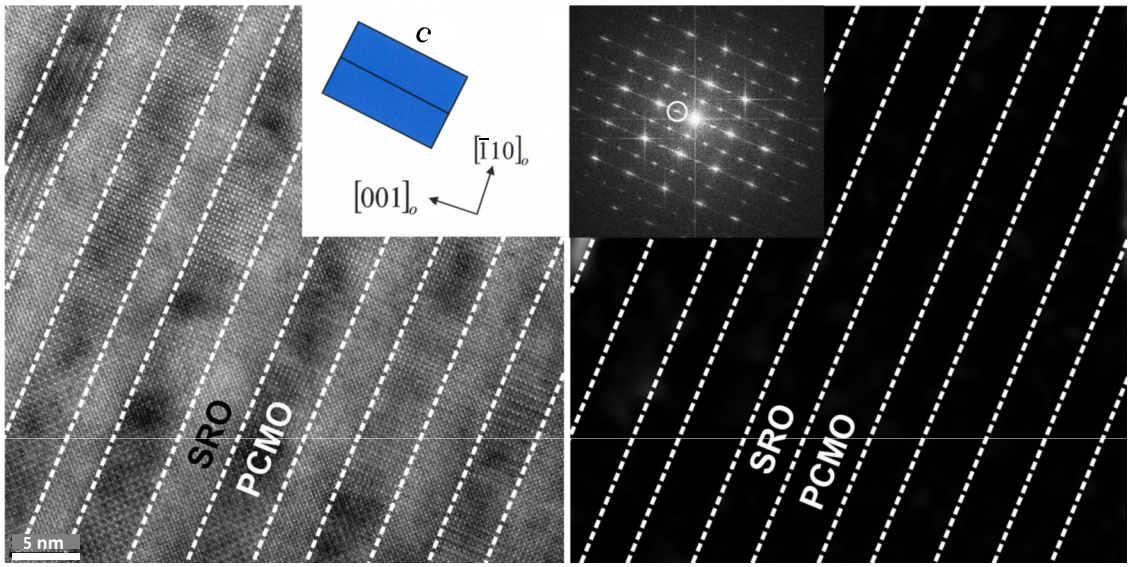

Figure 6. Sample SL3. Same as Fig. 5, but *with the out-of-plane orthorhombic c-axis perpendicular to the viewing direction.* Mind the scale bar (5 nm) in the bottom left corner.

mean that the orientation of the SRO layers was different from the one in sample SL1, whereas still being orthorhombic, the other two possible orientations were studied as well. As Fig. 5 shows, the reconstructed dark-field image in the light of the $(001)_o$ reflection (right) for the in-plane *c*-axis perpendicular to the viewing direction gives although non-zero, but still rather low intensity of the SRO layers. Figure 6 shows that the intensity of the SRO layers in the reconstructed dark-field image in the light of the $(001)_o$ reflection (right) for the orthorhombic SRO unit cell with out-of-plane *c*-axis was

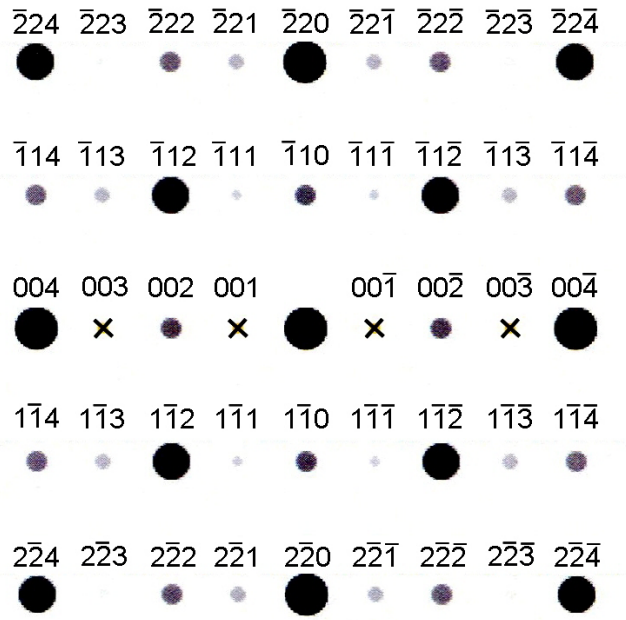

Figure 7. Simulated diffraction pattern for orthorhombic $SrRuO_3$. Zone axis $[110]_o$, i.e. in a direction corresponding to equivalent zone axes in Figs. 5 and 6. Kinematically forbidden but dynamically appearing reflections are marked by crosses, among them the $[001]_o$ reflection used during reconstruction of the dark-field images in those figures. Spot size is proportional to the intensity of the reflection. (Simulation performed by JEMS program [P. Stadelmann, EPFL Lausanne, Switzerland]).

zero. In result, the SRO layers in sample SL3 were either not orthorhombic, or contained only a very minor proportion of the orthorhombic phase. A corresponding FFT-based analysis of the HAADF-STEM images of the same two samples gave analogous results.

Figure 7 shows part of a simulated diffraction pattern of the orthorhombic SRO structure along the zone axis $[110]_o$, in particular revealing the $[001]_o$ reflections (indicated by crosses) used during reconstructed dark-field imaging in Figs. 5 and 6. Different from the FFT patterns in Figs. 3 to 6 which resulted from superpositions of the three SRO (and additionally PCMO) orientations shown in the insets of Figs. 4 to 6, Fig. 7 shows the diffraction pattern of only one single SRO orientation. The latter corresponds (slightly rotated) to the FFT pattern and schematic inset of Fig. 6. Although $[001]_o$ reflections are kinematically forbidden in the orthorhombic space group of SRO, they nevertheless appear due to dynamical diffraction conditions.

In all the Figs. 4 to 6 the SRO layers were dark, which means that they were not orthorhombic in sample SL3. Only occasionally, small spots of intensity could be seen in the SRO layers, which might indicate that there are very few orthorhombic domains in sample SL3. In conclusion, the SRO layers of sample SL1 were orthorhombic, whereas those in sample SL3 were either not orthorhombic or contain only very few orthorhombic domains.

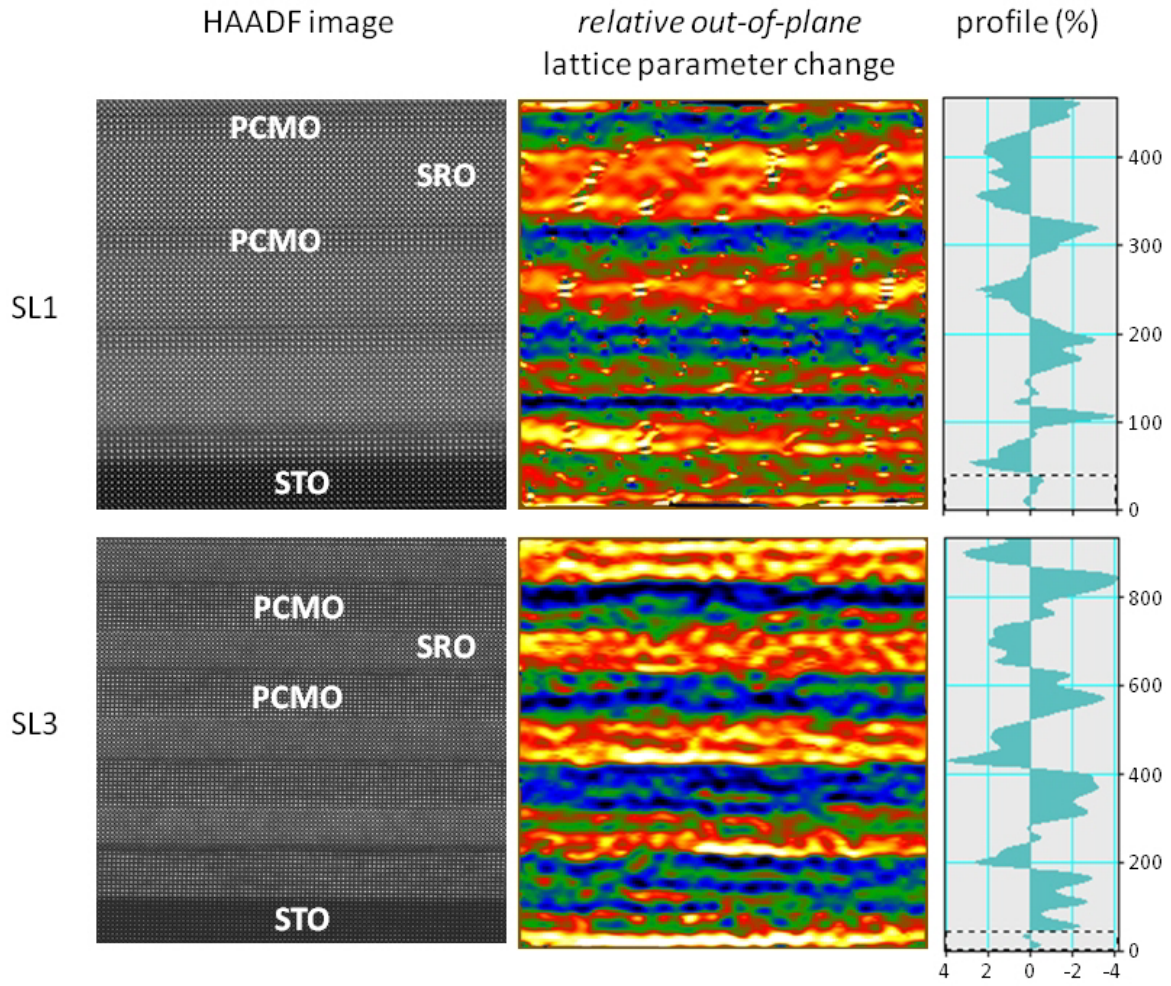

Figure 8. Profiles of the relative out-of-plane lattice parameter change of samples SL1 und SL3. Left: HAADF-images used for the analysis; center: maps of the relative out-of-plane lattice parameter deviation from the STO lattice constant; right: profile of the relative out-of-plane lattice parameter variation.

3.3. Strain analysis

The strain profiles of samples SL1 and SL3 were determined from both HAADF- and TEM-images; Fig. 8 shows the HAADF-images of samples SL1 and SL3 near the STO substrate that were analyzed. An analysis of the in-plane and out-of-plane atomic displacements, performed by applying the peak-pair analysis (which is a peak-finding method developed in [19]) to the HAADF images, showed fully strained PCMO and SRO layers. Thus, the in-plane lattice constants of both PCMO and SRO adapt to the STO lattice parameter. In the out-of-plane direction, relative to the STO lattice constant, the PCMO layers are compressed and the SRO layers are extended. This is presented in the map in the center part of Fig. 8 that shows the relative (with respect to STO) out-of-plane lattice parameter change as well as in the relative out-of-plane lattice parameter profiles on the right of Fig. 8. The changes in the out-of-plane lattice constants are

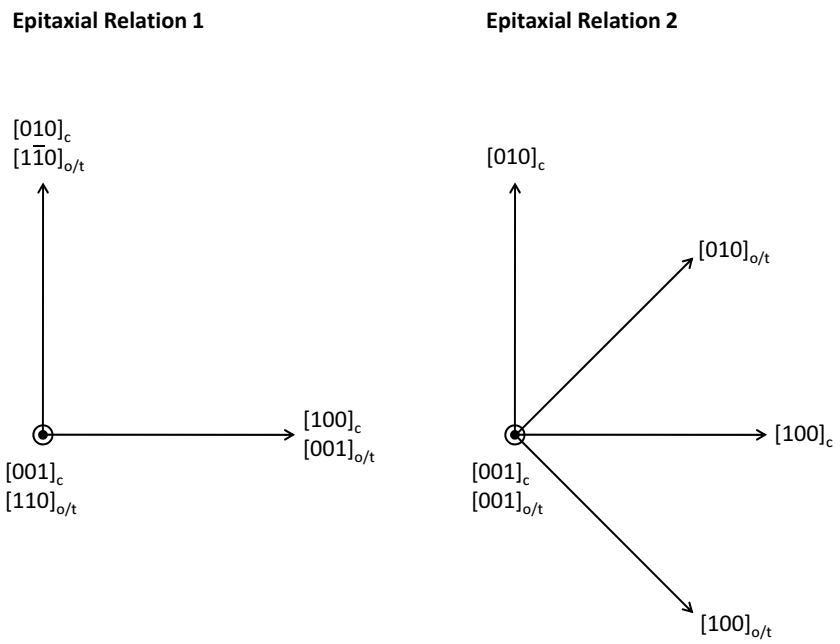

Figure 9. Sketch of the two epitaxial relations possible for the growth of orthorhombic (o) and tetragonal (t) $SrRuO_3$ films on $SrTiO_3(001)$ substrates. $[001]_c$ is along the growth direction of the film.

somewhat larger for the tetragonal sample SL3 than for the orthorhombic sample SL1; this is in agreement with the analysis of TEM-images. This might indicate that the structural transition is actually driven by strain. Since only one cross-section per sample was analyzed, it is impossible to determine the anisotropy of the in-plane strain. Therefore the pseudocubic lattice parameters of STO (a_{STO} = 0.3905 nm), PCMO (a_{PCMO} = 0.3850 nm) and SRO (a_{SRO} = 0.3923 nm) were used to estimate the strain values from the atomic displacements. This yielded in-plane strains of $\epsilon_{\parallel,PCMO} = 1.4\%$ and $\epsilon_{\parallel,SRO} = -0.5\%$ as well as out-of-plane strains $\epsilon_{\perp,PCMO} = -1.0\%$ and $\epsilon_{\perp,SRO} = 1.5\%$ for SL1 and $\epsilon_{\perp,PCMO} = -1.5\%$ and $\epsilon_{\perp,SRO} = 2.0\%$ for SL3. The relative error of this analysis is about 10-20%, partially induced by the choice of the STO reference area.

4. Magnetotransport properties

4.1. Theoretical considerations

In a ferromagnet, anisotropy energy and resistivity are functions of the direction of the spontaneous magnetization. Therefore, it is possible to conclude on the crystalline symmetry from direction-dependent measurements of the anisotropic magnetoresistance (AMR). The relevant equations for this approach are summarized in the appendix; the derivation followed Döring and Simon [20, 21].

The MR $\Delta\rho/\rho_0$ can be written as a function of a symmetric tensor of second rank

$(A_{ij})_{i,j=1,3}$ reduced by the directional unit vector $(\beta_1, \beta_2, \beta_3)$ of the current density [20]:

$$\Delta\rho/\rho_0 = \sum_{i,j=1}^{3} A_{ij}\beta_i\beta_j \,. \tag{1}$$

By definition the β_i are the direction cosines of the current density with respect to the crystallographic basis vectors. The tensor components A_{ij} are functions of the direction cosines of the magnetization, $\vec{M} = M_S\hat{m} = M_S(\alpha_1, \alpha_2, \alpha_3)$, where M_S denotes the saturation magnetization and $\hat{m}$ the unit vector along the magnetization direction. The functional form of the matrices $(A_{ij})_{i,j=1,3}$ was obtained from crystal symmetry considerations in [20, 21, 22].

In the following indices "c", "t" and "o" refer to the cubic directions of $SrTiO_3$ and to the tetragonal or orthorhombic directions of $SrRuO_3$, respectively. For $SrRuO_3$ either orthorhombic [15] or tetragonal [18] symmetry was assumed. The orthorhombic cell has four times the volume of the pseudocubic cell, i.e. in this cell the c-axis parameter and the basal plane area are doubled compared to the pseudocubic cell. The minimal tetragonal cell would have twice the volume of the pseudocubic cell [23]; for better comparison with the orthorhombic case [24], however, we chose a tetragonal cell also with four times the volume of the pseudocubic cell. We have mainly investigated two epitaxial relations for both orthorhombic and tetragonal symmetry. In the first epitaxial relation the $[001]_{o/t}$ axis is along the substrate $[100]_c$ axis, whereas the $[1\bar{1}0]_{o/t}$ axis is along the substrate $[010]_c$ axis, see Fig. 9(a). In the second epitaxial relation the $[001]_{o/t}$ axis is along the substrate $[001]_c$ axis, wheras the $[100]_{o/t}$ and $[010]_{o/t}$ axes are rotated with respect to the substrate $[100]_c$ and $[010]_c$ axes by 45 degrees, see Fig. 9(b). In case of single $SrRuO_3$ films grown on $SrTiO_3(001)$ substrates the first epitaxial relation is realized [14, 15]; macroscopic alignment of the orthorhombic $[001]_o$ axis along terrace steps is achieved by growth on slightly vicinal substrates. $SrRuO_3$ films grown on $SrTiO_3(001)$ in this fashion have a small monoclinic distortion with the angle between the orthorhombic a- and b-axes deviating from a right angle by about half a degree [15]. Therefore in case of this epitaxial relation also monoclinic symmetry is considered.

MR measurements were performed at constant magnetic field as a function of angle. For this the orientation of the substrate crystal was used as a reference system and angular sweeps in the $(100)_c$, $(010)_c$ and $(001)_c$ planes were performed. The direction of the magnetization vector with respect to the substrate crystal is specified by spherical coordinates, $\hat{m} = (\sin\theta\cos\varphi, \sin\theta\sin\varphi, \cos\theta)$ with the angles θ and φ defined with respect to the $[001]_c$ and $[100]_c$ axes, respectively. Note that the magnetization angles are not necessarily identical to the angles θ_F and φ_F between magnetic field and the substrate axes $[001]_c$ and $[100]_c$ that were directly measured. Accordingly the angles in out-of-plane field rotations are specified by θ_F and in in-plane field rotations by φ_F. The angular dependence of the anisotropic MR as determined from symmetry considerations was derived for the two epitaxial relations and the three rotation planes. Tetragonal, orthorhombic and monoclinic crystal structures are discussed; the relevant equations are summarized in the appendix.

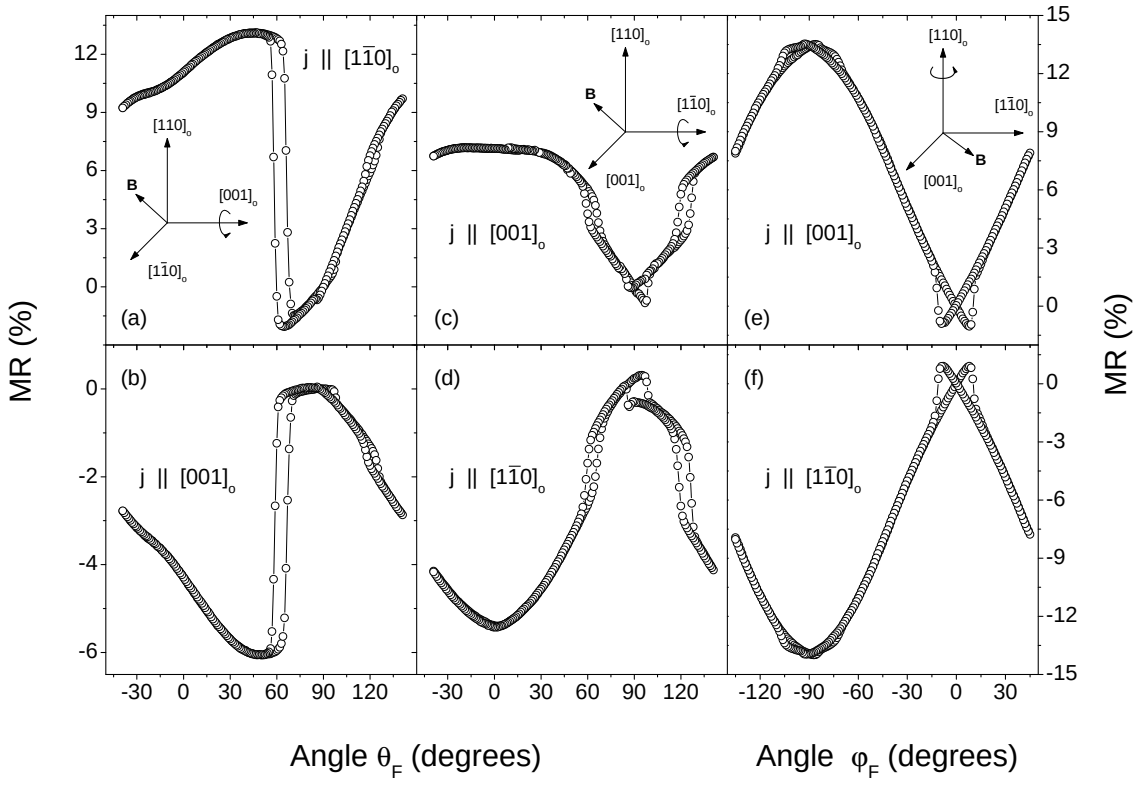

Figure 10. Sample SL1: $T = 10$ K, $\mu_0 H = 8$ T. Angular dependence of the magnetoresistance for magnetic field rotation in the $(001)_o$-, $(1\bar{1}0)_o$- and $(110)_o$-planes. The current directions are indicated in each panel. The insets indicate the rotation plane.

4.2. Angular magnetoresistance

The resistivity and the angular dependent MR of the three samples shown in Table 1 were measured. Since PCMO single layers are insulating [25], the resitivity and MR of the superlattices were entirely dominated by the SRO layers. Correspondingly, the resistivity vs. temperature curve of the PCMO/SRO SLs showed a slope change at the Curie temperature of the SRO layers [25], from which the Curie temperature of 143 K (as shown in Table 1) for the SRO layers was determined. The Curie temperature of the PCMO layers of 110-115 K was determined from magnetization measurements [26].

Here we only show angle dependent MR measurements, since these allow for the determination of the crystalline symmetry. The measurements were performed at various temperatures between 10 and 150 K. In the following the data for samples SL1 and SL3 at 10 and 130 K are shown. The angle dependence of the MR of sample SL2 had the same form as that of sample SL3. Figure 10 shows the MR of sample SL1 measured at 10 K. The MR shows hysteresis for certain angles that indicates the presence of a magnetically hard axis close to the corresponding direction. Since SRO has a large magnetocrystalline anisotropy [14], even at 8 T the magnetization and magnetic-field direction do not agree at low temperatures. In case of sample SL1 the direction of two magnetically hard axes is clearly identified. One lies in the $(001)_o$-plane at about 60

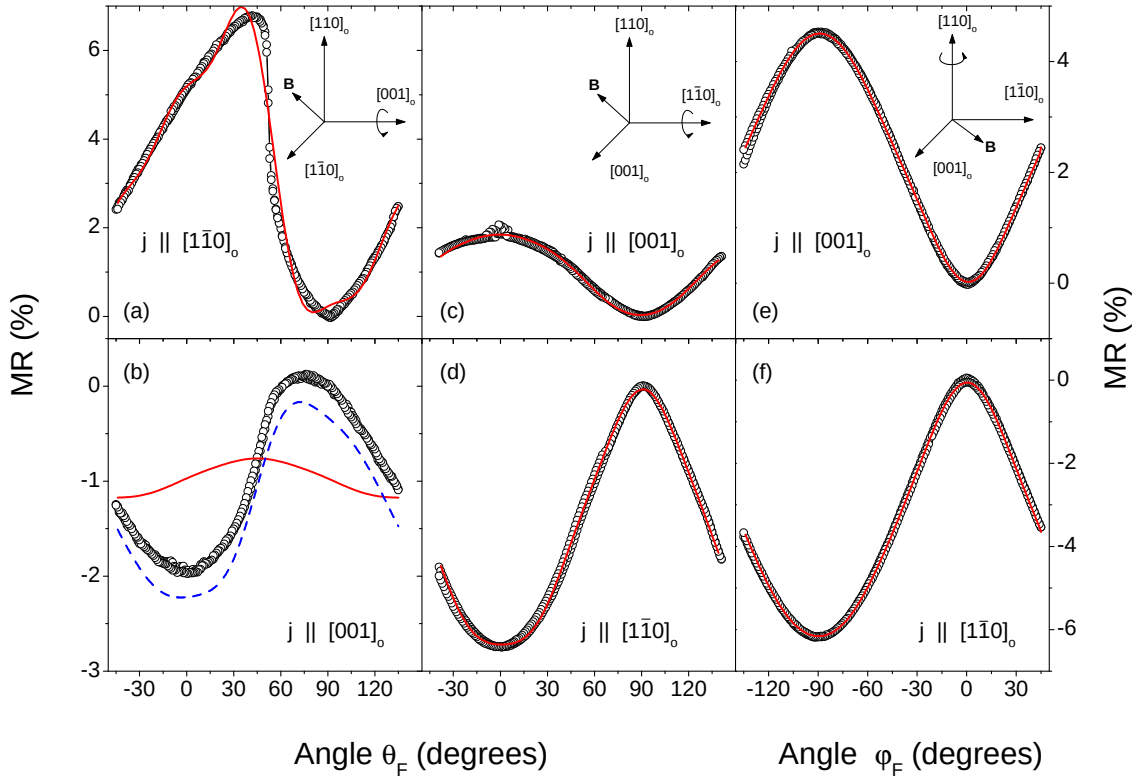

Figure 11. Sample SL1: $T = 130$ K, $\mu_0 H = 8$ T. Angular dependence of the magnetoresistance for magnetic field rotation in the $(001)_o$-, $(1\bar{1}0)_o$- and $(110)_o$-planes. The current directions are indicated in the figure. The solid red lines are fits of Eqs. (5-9) for orthorhombic symmetry to the data. The dashed blue curve is a fit of Eq. (10) for monoclinic symmetry to the data; for clarity this curve was downshifted by -0.3% (absolute).

degrees from the $[110]_o$ direction, see sharp hysteretic MR jump in Figs. 10(a) and (b); the second is along the $[001]_o$ axis, see hysteresis close to $\theta_F = 0$ in Fig. 10(c) and (d) and $\varphi_F = 0$ in Figs. 10(e) and (f). The magnetic hard axes directions are characteristic for *orthorhombic* SRO films grown on $SrTiO_3(001)$ [14, 27]. Further, comparing the angular MR traces of sample SL1 with the data of the 40 nm thick $SrRuO_3$ single film presented in [14], it is immediately evident that the SRO layers in sample SL1 have orthorhombic, actually monoclinic, symmetry. Fitting of the experimental data at 10 K is difficult, since the magnetocrystalline anisotropy energy of the SRO layers is not accurately known and therefore the relation between magnetization angles (θ, φ) and magnetic field angles (θ_F, φ_F) is difficult to determine. However, at higher temperatures, the thermal fluctuations are larger and the magnetocrystalline energy might be smaller and the MR curves are smooth, see the MR data of sample SL1 at 130 K in Fig. 11. Thus one might assume $\theta \simeq \theta_F$ and $\varphi \simeq \varphi_F$. Eqs. (5-9) derived for orthorhombic symmetry accurately fit the data in Figs. 11(a) and (c)-(f), but not (b), see solid red lines; for the fitting the expressions Eqs. (5-9) were truncated at eighth order. This is in agreement with the results for a single SRO film in [14]. The MR curve in Fig. 11(b) cannot

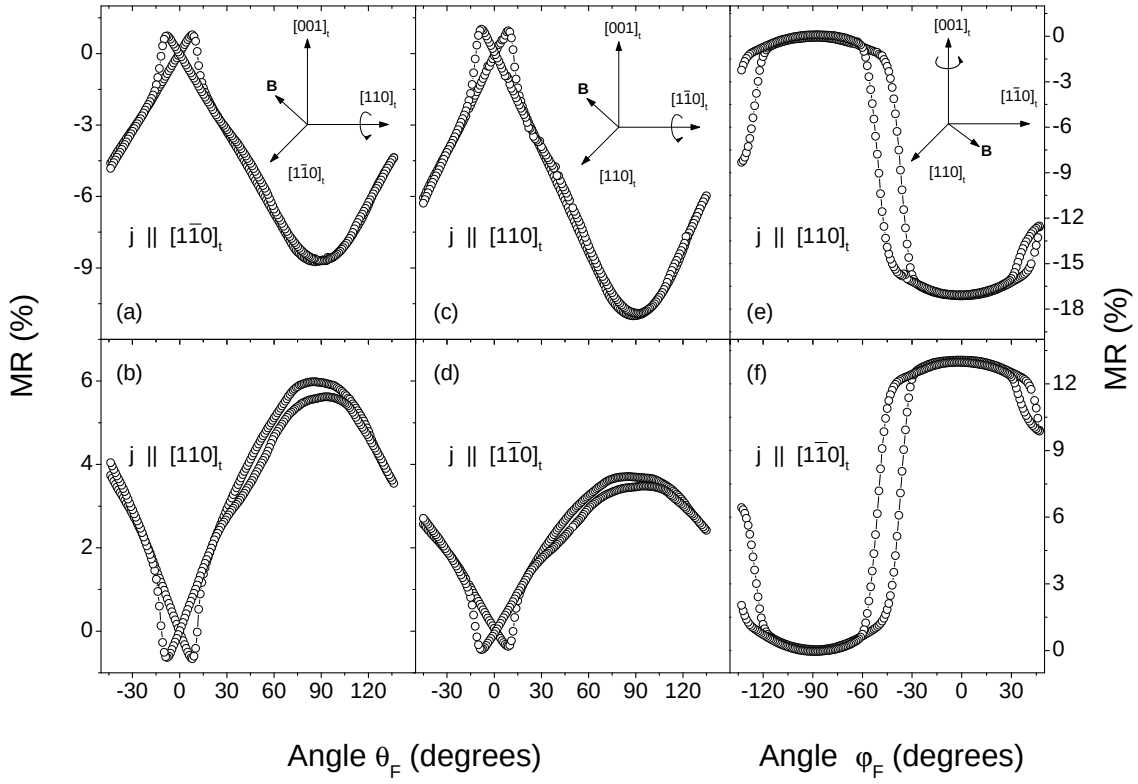

Figure 12. Sample SL3: $T = 10$ K, $\mu_0 H = 8$ T. Angular dependence of the magnetoresistance for magnetic field rotation in the $(110)_t$-, $(1\bar{1}0)_t$- and $(001)_t$-planes. The current directions are indicated in each panel.

be described by Eq. (6) even if higher order terms were taken into account, since the experimental data contain a large $\cos(2\theta)$ term absent in Eq. (6). The corresponding expression for monoclinic symmetry, Eq. (10), contains this term and fits the data in Fig. 11(b) well, see dashed blue line. This result is again in agreement with the SRO single film results [14] and is consistent with the fact that a monoclinic distortion between *a*- and *b*-axes was observed in SRO films [15, 28]. Since the MR data cannot be understood within the other epitaxial relations and crystalline symmetries, from the MR analysis we firmly conclude that the crystalline symmetry of the SRO layers of sample SL1 is orthorhombic (monoclinic). This is in full agreement with the HRTEM results discussed in section 3.

Figure 12 shows the angular MR of sample SL3 measured at 10 K. Comparison with Fig. 10 shows that the form of the angular dependence is significantly different from the orthorhombic case with the *c*-axis in-plane. In case of sample SL3 hysteresis occurs close to the surface normal, $\theta_F = 0$ degrees, see Figs. 12(a)-(d) and in case of in-plane rotations near $\varphi_F = -45$ degrees, see Figs. 12(e)-(f). Accordingly, compared to sample SL1 the SRO layers in sample SL3 have another orientation, another crystalline symmetry or both. Since the form of the MR curves in Figs. 12(a) and (c) as well as (b) and (d) are very similar, it appears probable that the *c*-axis of the either tetragonal or orthorhombic structure is along the SL normal, i.e. that the second epitaxial relation shown in Fig. 9

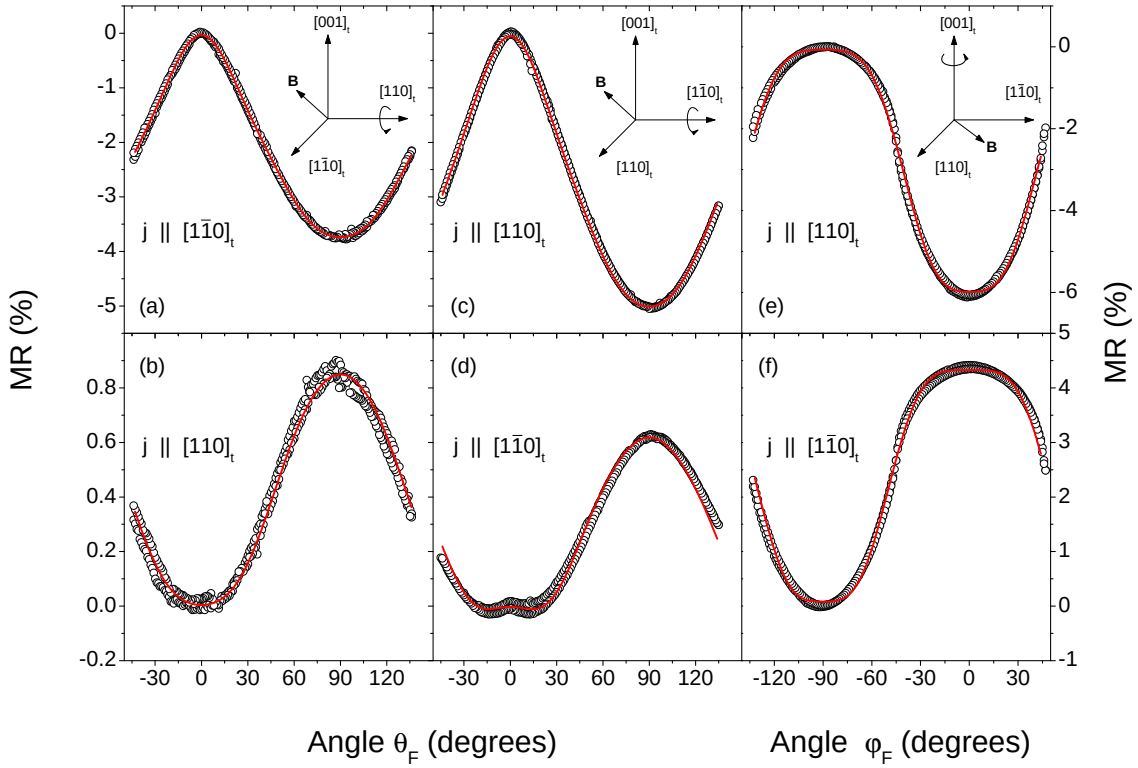

Figure 13. Sample SL3: $T = 130$ K, $\mu_0 H = 8$ T. Angular dependence of the magnetoresistance for magnetic field rotation in the $(110)_t$-, $(1\bar{1}0)_t$- and $(001)_t$-planes. The current directions are indicated in the figure. The solid red lines are fits of Eqs. (11-13) for tetragonal symmetry to the data.

Table 2. Coefficients of Eqs. (12,13) for samples SL2 and SL3 and of Eqs. (8,9) for sample SL1 at 130 K.

	SL2		SL3		SL1	
$2n$	c_{2n}^{t1} (10^{-4})	c_{2n}^{t2} (10^{-4})	c_{2n}^{t1} (10^{-4})	c_{2n}^{t2} (10^{-4})	c_{2n}^{o1} (10^{-4})	c_{2n}^{o2} (10^{-4})
0	−229	+341	−280	+239	+237.8	−341.0
2	−271	+349	−328	+238	−216.0	+296.9
4	−25.3	−26.3	−28.7	−24.3	−9.5	+27.4
6	+30.0	−40.9	+31.9	−25.8	−8.3	+8.5
8	+7.3	+6.2	+6.0	+5.4	−2.0	+3.0

is realized for sample SL3. The out-of-plane rotations shown in Fig. 12(a)-(d), however, do not allow for a discrimination of orthorhombic and tetragonal symmetry, since these rotations occur in the $[110]_{o/t}$ and $[\bar{1}10]_{o/t}$ planes that have equivalent symmetry in the two crystallographic structures.

Since the magnetocrystalline anisotropy energy of the SRO layers in sample SL3 is very large, fits of Eqs. (11-13) were made to the MR data of sample SL3 at 130 K. These fits are shown by the red lines in Fig. 13; as above the expressions were truncated

at eighth order. The fitting of the curves to the data is fully convincing. However, since the functional form of the MR in Eqs. (11-13) is the same for orthorhombic and tetragonal symmetry, this agreement does not yet discriminate between the two crystalline structures. A discrimination is, however, possible by an analysis of the expansion coefficients in the expressions for the in-plane rotation. In case of tetragonal symmetry, the coefficients c_{2n}^{t1} and c_{2n}^{t2} for the two current-density directions have a definite relationship: $c_{4n}^{t2} = c_{4n}^{t1}$, $c_{4n-2}^{t2} = -c_{4n-2}^{t1}$, $n = 1, 2, 3...$, whereas the corresponding coefficients for the orthorhombic symmetry are independent of each other. The coefficients obtained at 130 K are shown for samples SL2 and SL3 as well as – for comparison – for sample SL1 in Table 2. In case of the first two samples the coefficients indeed show the alternating $+/-$ pattern as predicted for tetragonal symmetry, see Eqs. (12,13), whereas the corresponding coefficients obtained for sample SL1 do not show this pattern, see rightmost two columns of Table 2. Therefore we conclude from the angular dependent MR measurements that the SRO layers in samples SL2 and SL3 have tetragonal symmetry with the c-axis along the SL normal.

Since from Fig. 6, the absence of the orthorhombic SRO orientation with the c-axis parallel to the growth direction has been deduced for sample SL3, and from Fig. 13 the c-axis of either the tetragonal or the orthorhombic phase has been deduced to be parallel to the growth direction in this sample, we can clearly conclude that in sample SL3 there is a tetragonal phase present with its c-axis parallel to the growth direction. We cannot firmly exclude, however, the existence of tetragonal domains with an in-plane c-axis.

5. Conclusions

In this work we have shown by a combination of two techniques, namely high-resolution transmission electron microscopy and angular dependent magnetoresistance measurements, that the $SrRuO_3$ layers in a $Pr_{0.7}Ca_{0.3}MnO_3/SrRuO_3$ superlattice undergo a phase transition from orthorhombic to tetragonal structure, when the thickness of the PCMO layers is increased from 1.5 to 4 nm. The orthorhombic c-axis of the SRO layers was found to lie in-plane, whereas the tetragonal c-axis of the SRO layers seemed to be oriented along the SL normal; for the tetragonal orientation, however, the existence of crystallographic domains with in-plane c-axis cannot be fully excluded. The results impressively demonstrate that this structural phase transition has a large impact on the magnetotransport properties. This is surprising, since the actual atomic displacements between the phases are rather small.

What drives this phase transition? An obvious candidate in case of thin films and superlattices is strain. Indeed, the transition temperature for the orthorhombic(O)-to-tetragonal(T) transition was found to be substantially lowered in compressively strained SRO films grown on $SrTiO_3$(001) [28, 29]. Since PCMO has an even smaller lattice constant than STO, a further lowering of the OT-transition temperature might be expected; furthermore, the strain exerted by the PCMO layers is not biaxial, but anisotropic, which might also modify the strain effect. Since we observed the tetragonal

structure of the SRO layers down to 10 K, this would mean that the strain effect had lowered the OT-transition temperature basically to zero. The properties of strained $SrRuO_3$ films were studied by first principles calculations without any hints of a structural transition [30]. On the other hand, experimental studies on single SRO films showed monoclinic structure under compressive and tetragonal structure under tensile strain [31]. The present result of an OT-transition of the SRO layers under overall compressive strain highlights another facet of this intricate structural problem. Probably an explanation in terms of strain effects alone is not sufficient. In an alternative scenario the OT-transition might be influenced by the electronic or magnetic coupling between the PCMO and SRO layers. Here it would be interesting for future research to look for structural anomalies in these superlattices near the magnetic transition at 110 K and the charge ordering transition near 240 K [32].

Acknowledgments

This work was supported by the German Science Foundation (DFG) within the Collaborative Research Center SFB 762 "Functionality of Oxide Interfaces". We thank Dr. J. Henk for a careful reading of the manuscript.

Appendix

The unit vector of the magnetization in the system of the $SrTiO_3$ substrate crystal is written as $\hat{m} = (\sin\theta\cos\varphi, \sin\theta\sin\varphi, \cos\theta)$ such that θ is the angle between the magnetization and $[001]_c$ and φ is the angle between the magnetization and $[100]_c$. The direction cosines of the magnetization $(\alpha_1, \alpha_2, \alpha_3)$ and the current density $(\beta_1, \beta_2, \beta_3)$ are defined with respect to the crystallographic axes of the SRO film.

The formulas below just indicate the structure of the solutions. Unless indicated otherwise the coefficients in the equations – although throughout denoted by c_{2n} and s_{2n} – are different for the various rotation planes and current directions. Miller indices (hkl) specify the rotation plane, the direction vector $[uvw]$ specifies the corresponding current density direction.

5.1. Epitaxial Relation 1, tetragonal symmetry (D_{4h})

5.1.1. $(100)_c/(001)_t$, $[1\bar{1}0]_t$. $(010)_c/(1\bar{1}0)_t$, $[001]_t$. $(010)_c/(1\bar{1}0)_t$, $[1\bar{1}0]_t$.

$$\Delta\rho/\rho_0 = c_0 + \sum_{n=1}^{\infty} c_{2n}\cos(2n\theta)\,. \tag{2}$$

5.1.2. $(100)_c/(001)_t$, $[001]_t$.

$$\Delta\rho/\rho_0 = c_0 + \sum_{n=1}^{\infty} c_{4n}\cos(4n\theta)\,. \tag{3}$$

5.1.3. $(001)_c/(110)_t$, $[001]_t$. $(001)_c/(110)_t$, $[1\bar{1}0]_t$.

$$\Delta\rho/\rho_0 = c_0 + \sum_{n=1}^{\infty} c_{2n}\cos(2n\varphi)\,. \tag{4}$$

5.2. Epitaxial Relation 1, orthorhombic symmetry (D_{2h})

5.2.1. $(100)_c/(001)_o$, $[1\bar{1}0]_o$.

$$\Delta\rho/\rho_0 = c_0 + \sum_{n=1}^{\infty} s_{2n}\sin(2n\theta) + \sum_{n=1}^{\infty} c_{2n}\cos(2n\theta)\,. \tag{5}$$

5.2.2. $(100)_c/(001)_o$, $[001]_o$.

$$\Delta\rho/\rho_0 = c_0 + \sum_{n=1}^{\infty} s_{4n-2}\sin\left((4n-2)\theta\right) + \sum_{n=1}^{\infty} c_{4n}\cos(4n\theta)\,. \tag{6}$$

5.2.3. $(010)_c/(1\bar{1}0)_o$, $[001]_o$. $(010)_c/(1\bar{1}0)_o$, $[1\bar{1}0]_o$.

$$\Delta\rho/\rho_0 = c_0 + \sum_{n=1}^{\infty} c_{2n}\cos(2n\theta)\,. \tag{7}$$

5.2.4. $(001)_c/(110)_o$, $[001]_o$.

$$\Delta\rho/\rho_0 = c_0^{o1} + \sum_{n=1}^{\infty} c_{2n}^{o1}\cos(2n\varphi)\,. \tag{8}$$

5.2.5. $(001)_c/(110)_o$, $[1\bar{1}0]_o$.

$$\Delta\rho/\rho_0 = c_0^{o2} + \sum_{n=1}^{\infty} c_{2n}^{o2}\cos(2n\varphi)\,. \tag{9}$$

5.3. Epitaxial Relation 1, monoclinic symmetry (C_{2h})

Compared to the orthorhombic symmetry there is only one modification:

5.3.1. $(100)_c/(001)_m$, $[001]_m$.

$$\Delta\rho/\rho_0 = c_0 + \sum_{n=1}^{\infty} s_{2n}\sin(2n\theta) + \sum_{n=1}^{\infty} c_{2n}\cos(2n\theta)\,. \tag{10}$$

5.4. Epitaxial Relation 2, tetragonal symmetry (D_{4h})

5.4.1. $(100)_c/(110)_t$, $[\bar{1}10]_t$. $(100)_c/(110)_t$, $[110]_t$. $(010)_c/(\bar{1}10)_t$, $[110]_t$. $(010)_c/(\bar{1}10)_t$, $[\bar{1}10]_t$.

$$\Delta\rho/\rho_0 = c_0 + \sum_{n=1}^{\infty} c_{2n}\cos(2n\theta)\,. \tag{11}$$

Note that the coefficients in the expression for the first and third as well as the second and fourth configuration are the same.

5.4.2. $(001)_c/(001)_t$, $[110]_t$.

$$\Delta\rho/\rho_0 = c_0^{t1} + \sum_{n=1}^{\infty} c_{2n}^{t1}\cos(2n\varphi)\,. \tag{12}$$

5.4.3. $(001)_c/(001)_t$, $[\bar{1}10]_t$.

$$\Delta\rho/\rho_0 = c_0^{t2} + \sum_{n=1}^{\infty} c_{2n}^{t2}\cos(2n\varphi)\,. \tag{13}$$

Note that $c_{4n}^{t2} = c_{4n}^{t1}$, $c_{4n-2}^{t2} = -c_{4n-2}^{t1}$, $n = 1, 2, 3....$

5.5. Epitaxial Relation 2, orthorhombic symmetry (D_{2h})

For orthorhombic symmetry the equations for the out-of-plane rotation configurations have the same structure as the corresponding ones for tetragonal symmetry specified in the preceding section. This comes from the fact that the choice of rotation planes to be the $(100)_c$ and $(010)_c$ planes does not allow for a discrimination of the orthorhombic *a*- and *b*-axes which are under 45 degrees with respect to the rotation planes. The symmetry of the in-plane rotation, however, leads to different expansions.

5.5.1. $(001)_c/(001)_o$, $[110]_o$. $(001)_c/(001)_o$, $[\bar{1}10]_o$.

$$\Delta\rho/\rho_0 = c_0 + \sum_{n=1}^{\infty} s_{2n}\sin(2n\varphi) + \sum_{n=1}^{\infty} c_{2n}\cos(2n\varphi)\,. \tag{14}$$

References

[1] Reyren N, Thiel S, Caviglia A D, Fitting-Kourkoutis L, Hammerl G, Richter C, Schneider C W, Kopp T, Ruetschi A S, Jaccard D, Gabay M, Muller D A, Triscone J M and Mannhart J 2007 *Science* **317** 1196

[2] Gajek M, Bibes M, Fusil S, Bouzehouane K, Fontcuberta J, Barthélémy A and Fert A 2007 *Nature Materials* **6** 296

[3] Vrejoiu I, Ziese M, Setzer A, Esquinazi P, Birajdar B I, Lotnyk A, Alexe M and Hesse D 2008 *Appl. Phys. Lett.* **92** 152506

[4] Ziese M, Vrejoiu I, Pippel E, Esquinazi P, Hesse D, Etz C, Henk J, Ernst A, Maznichenko I V, Hergert W and Mertig I 2010 *Phys. Rev. Lett.* **104** 167203

[5] Ziese M, Vrejoiu I and Hesse D 2010 *Appl. Phys. Lett.* **97** 052504
[6] Ke X, Rzchowski M S, Belenky L J and Eom C B 2004 *Appl. Phys. Lett.* **84** 5458
[7] Ke X, Belenky L J, Eom C B and Rzchowski M S 2005 *J. Appl. Phys.* **97** 10K115
[8] Padhan P, Prellier W and Budhani R C 2006 *Appl. Phys. Lett.* **88** 192509
[9] Lee Y, Caes B and Harmon B 2008 *Journal of Alloys and Compounds* **450** 1–6
[10] Cao G, McCall S, Shepard M, Crow J E and Guertin R P 1997 *Phys. Rev. B* **56** 321–329
[11] Klein L, Dodge J S, Ahn C H, Snyder G J, Geballe T H, Beasley M R and Kapitulnik A 1996 *Phys. Rev. Lett.* **77** 2774
[12] Jirák Z, Krupička S, Šimša Z, Dlouhá M and Vratislav S 1985 *J. Magn. Magn. Mater.* **53** 153
[13] Yoshizawa H, Kawano H, Tomioka Y and Tokura Y 1995 *Phys. Rev. B* **52** R13145
[14] Ziese M, Vrejoiu I and Hesse D 2010 *Phys. Rev. B* **81** 184418
[15] Gan Q, Rao R A, Eom C B, Wu L and Tsui F 1999 *J. Appl. Phys.* **85** 5297
[16] Scherzer O 1949 *J. Appl. Phys.* **20** 20
[17] Fujimoto M, Koyama H, Nishi Y, Suzuki T, Kobayashi S, Tamai Y and Awaya N 2007 *J. Am. Ceram Soc.* **90** 2205
[18] Vailionis A, Siemons W and Koster G 2008 *Appl. Phys. Lett.* **93** 051909
[19] Galindo P, Kret S, Sanchez A M, Laval J Y, Yanez A, Pizarro J, Guerrero E, Ben T and Molina S 2007 *Ultramicroscopy* **107** 186
[20] Döring W and Simon G 1960 *Ann. Physik* **460** 373–387
[21] Döring W and Simon G 1961 *Ann. Physik* **463** 144–145
[22] Döring W 1957 *Ann. Physik* **456** 102–109
[23] Zakharov N D, Satyalakshmi K M, Koren G and Hesse D 1999 *J. Mater. Research* **14** 4385
[24] Kennedy B J and Hunter B A 1998 *Phys. Rev. B* **58** 653
[25] Ziese M, Vrejoiu I, Pippel E and Hesse D 2011 *unpublished*
[26] Ziese M, Vrejoiu I, Pippel E, Nikulina E and Hesse D 2011 *Appl. Phys. Lett.* **98** 132504
[27] Kolesnik S, Yoo Y Z, Chmaissem O, Dabrowski B, Maxwell T, Kimball C W and Genis A P 2006 *J. Appl. Phys.* **99** 08F501
[28] Vailionis A, Siemons W and Koster G 2007 *Appl. Phys. Lett.* **91** 071907
[29] Choi K J, Baek S H, Jang H W, Belenky L J, Lyubchenko M and Eom C B 2010 *Adv. Mater.* **22** 759
[30] Zayak A T, Huang X, Neaton J B and Rabe K M 2006 *Phys. Rev. B* **74** 094104
[31] Vailionis A, Boschker H, Siemons W, Houwman E P, Blank D H A, Rijnders G and Koster G 2011 *Phys. Rev. B* **83** 064101
[32] Tomioka Y, Asamitsu A, Kuwahara H, Moritomo Y and Tokura Y 1996 *Phys. Rev. B* **53** R1689